Comparative Modal Analysis of Beam-Plate Coupled Models for Isotropic Active Camber Morphing Wings

Ke Huang[1], Jiaying Zhang[1,*]

[1] School of Aeronautic Science and Engineering, Beihang University, Beijing 100190, China

E-mail: jiaying.zhang@buaa.edu.cn

Abstract. For structures with rigid-flexible coupling, such as active camber morphing wings, traditional beam and plate models for conventional wings have some limitations, especially to capture both chord-wise flexibility and torsional effects at the same time accurately and efficiently. This paper aims to address this gap and improve the prediction of natural frequencies and vibration modes for such morphing wing structures. The natural frequencies and vibration modes of three isotropic cantilever beams models, i.e., varying aspect ratios (AR), stepped cantilever beams with different ARs and with different morphing segment ratio, are experimentally measured by Scanning Laser Doppler vibrometry (SLDV), and compared with finite element (FEM) model results. For conventional wings, the plate model is more accurate for small AR wings, while the beam model performs better for large AR wing. However, in camber morphing wings with varying geometries, using the beam model for the stiff sections and the plate model for the flexible sections can achieve the highest accuracy and efficiency. The reason is that combined beam-plate model effectively captures the chordwise bending of the flexible trailing edge and the spanwise bending and torsion of the rigid leading edge. The results provide a theoretical foundation for simplified equivalent models of rigid-flexible coupled structures, especially for active camber morphing wings.

Keywords. Morphing aircraft, Active camber morphing wings, Rigid-flexible coupled, Scanning laser Doppler vibrometry, Equivalent wing structural models

1. Introduction

Morphing aircraft structures must be flexible to optimize aerodynamic performance over diverse operating conditions while maintaining sufficient rigidity to bear aerodynamic and maneuvering loads[1]. The concept of morphing aircraft is developing a single aircraft capable of performing various missions and adapting to different flight conditions, rather than relying on multiple specialized aircraft [2]. Based on the dimensions in wing deformation, which change with flight conditions and missions, morphing wings can be classified into planar deformation [3-6], out-of-plane deformation [7-10], and aerofoil deformation [11-15].

Camber morphing wings have widely appreciated in the aeronautics community due to their easier integration compared to large-scale deformations like variable span and swept wings. They can directly replace traditional discrete control surfaces, simplifying design and experimental validation [16, 17]. Studies have shown that camber morphing wings offer several aerodynamic advantages, including smooth aerodynamic surfaces, reduced induced drag, and high aerodynamic and drive efficiency [18-21].

Analytical methods with finite elements (FEM) are often used in traditional aircraft modelling, and most of them are based on the Rayleigh method and discretization methods [22]. An equivalent plate model is always used for static and dynamic analysis of wing structures, which is composed of skins, spars, and ribs [23, 24]. This physical equivalent model, allows for early evaluation in the design stage, simplifying structural discontinuities to improve computational efficiency in design and optimization. As a result, it can also be applied to modelling and analysing the driving characteristics of structures with morphing trailing edges [25]. Simplifying the wing into a stick model for aeroelastic analysis is also widely used in some aircraft modelling [26-28].

When selecting models, the choice of elements must evaluate accuracy and computational efficiency to meet specific requirements. Using highly-fidelity 3D shell models without any structural simplification for every design case at the late conceptual and early preliminary design stages is impractical. For realistic wing structures, modal characteristics are usually analyzed using detailed three-dimensional finite element models without structural simplification. These models also serve as the basis for structural model reduction [29]. For example, Zou and Huang [30] studied a folding-wing aircraft that had completed ground vibration tests. They constructed a finite element model using the actual wing structure and material properties. A reduced-order model was then derived from the full three-dimensional model to analyze the aeroelastic response. Zhao et al. [31] designed a composite flying-wing aircraft and performed finite element model updating using multi-level optimization based on ground vibration test data. A similar procedure was applied in the study of the X-56A aircraft. The finite element model was iteratively refined following NASA standards until the numerical frequencies and mode shapes agreed with ground vibration test results within acceptable error bounds [32]. Avin et al.

[33] used the Pazy wing as a benchmark for geometrically nonlinear aeroelastic analysis. The Pazy wing consists of a thin aluminum spar and a Nylon 12 printed rib chassis that provides the NACA0018 airfoil shape. A finite element model representing the real wing structure was constructed and validated through modal analysis in Nastran. The numerical aeroelastic results were further compared with wind-tunnel experiments. Based on this wing, Riso and Cesnik [34] further investigated a low-order modeling approach using beam-element model condensation. They showed that this model maintains high accuracy in aeroelastic and nonlinear large-deformation analyses and provides appropriate-fidelity modeling choices for wing design and optimization.

Reducing complex three-dimensional finite element models to one-dimensional beam models through model condensation is a common modeling approach [35]. It has been applied to flying-wing configurations [36] and morphing-wing trailing edges [37]. Such simplified models capture the dominant inertia and stiffness characteristics while neglecting internal structural details. This approach significantly improves the efficiency of subsequent flight-dynamics and aeroelastic computations. Low-order models are not only useful for design and optimization but also valuable for parametric studies and flutter-mechanism investigations [38]. For example, in a parametric study of a morphing-wing trailing edge, Pecora et al. [36] simplified the detailed shell model of a complex wing box using beam elements and lumped masses. This beam-equivalent model significantly improved the efficiency of subsequent multi-parametric flutter analysis. In another study, Zou and Huang [39] investigated the mechanism of body-freedom flutter using strong structural simplifications. The wing and fuselage were reduced to two-dimensional stiffness representations connected by lumped springs. This reduced-order rigid-elastic aeroelastic model clearly explained the flutter mechanism observed in experiments.

Instead, a suitable equivalent continuum model should be chosen based on geometry and deformation characteristics [24]. For wings with an aspect ratio (AR) greater than 5, a one-dimensional beam model is sufficient. For wings with lower ARs, where spanwise and chordwise components of the normal stress assume nearly equal proportions, the plate model offers greater accuracy [40-42]. These approaches suitable for large chordwise stiffness under the rigid wing assumption, and Theodorsen's theory of unsteady aerodynamics for thin airfoils is therefore valid [43, 44]. However, if the airfoils are flexible in the chordwise direction, chordwise deflection must be considered, which will break the rigid airfoil assumption. In such cases, the application of beam theory should be re-evaluated [45, 46].

In modelling morphing trailing edge airfoils using equivalent plate theory, both rigid and flexible sections should be unified based on energy equivalence, which is simplifying the 3D structure to a 2D variable stiffness plate model [25]. Comparisons with 3D shell models show that the equivalent plate model provides high accuracy in the mechanical response. For the ACTE flap, a plate model is integrated into a reference bar model using beam elements, and ground vibration tests confirm that the plate-beam coupled model is highly accurate [47]. However, no study has yet compared these two

models directly. Most studies treat the rigid part as fully rigid and ignore the elasticity of the wing spar, focusing only on the deformation of the trailing edge [48, 49]. Such assumption of rigidity is no longer valid when the structures towards more flexible, lightweight[38], and there is increasing interest in modelling morphing wings with flexible trailing edges and accounting for bending and torsional coupling deformations in the elastic spars [50, 51]. Therefore, a universal way is needed on selecting the appropriate model for the structural analysis of 3D rigid-flexible coupled morphing wings, especially for subsequent aeroelastic and rigid-flexible coupled flight dynamics modelling.

In this paper, a rectangular cantilever plate, commonly used in wind tunnel testing and preliminary design, is adopted as a simple geometry to capture the relevant physical phenomena [52]. Additionally, a cantilevered stepped variable-thickness beam [53] is used to simulate a rigid-flexible coupled structure, capturing the stiffness variations in different parts. This study proposes a beam–plate coupled model that balances computational accuracy and efficiency. It accurately predicts cantilevered stepped plate modes consistent with the stiffness distribution of camber morphing wings, with experimental validation using scanning laser Doppler vibrometry (SLDV). This study is based on several assumptions and simplifications. The material is assumed to be linear-elastic and isotropic. The wing is modeled as a simplified rectangular structure. Complex internal structures and detailed aerodynamic geometry are neglected. The analysis is limited to linear modal analysis under small-amplitude vibrations. Therefore, the conclusions are applicable to the preliminary design and modal analysis stage of simplified structures. Extrapolation to composite materials, nonlinear behavior, and realistic wing geometries requires further validation.

This paper is organized as follows. Section 2 presents the structural models. Section 3 details the material characterization and experimental arrangement. Section 4 details the different finite-element models and numerical settings. Section 5 provides a nondimensional comparison between experimental and numerical results. Section 6 examines discrepancies among models in terms of their underlying structural assumptions and traces the sources of error. Section 7 concludes with the limitations of the present study and directions for future work. Figure 1 depicts the overall research workflow.

Contributions of this work

- A beam-plate coupled modeling approach is proposed and validated for rigid-flexible coupled morphing wing structures, balancing computational accuracy and efficiency.
- Systematic comparisons of beam-beam, beam-plate, and plate-plate models are performed over a range of aspect ratios (AR = 3–6) and flexible segment ratios (f_{ef} = 25%–75%).
- Model selection guidelines are established based on quantitative error analysis and computational cost, providing practical recommendations for different design stages.
- Experimental validation using SLDV and material characterization quantifies the effects of manufacturing tolerances and material uncertainty on modal frequencies.

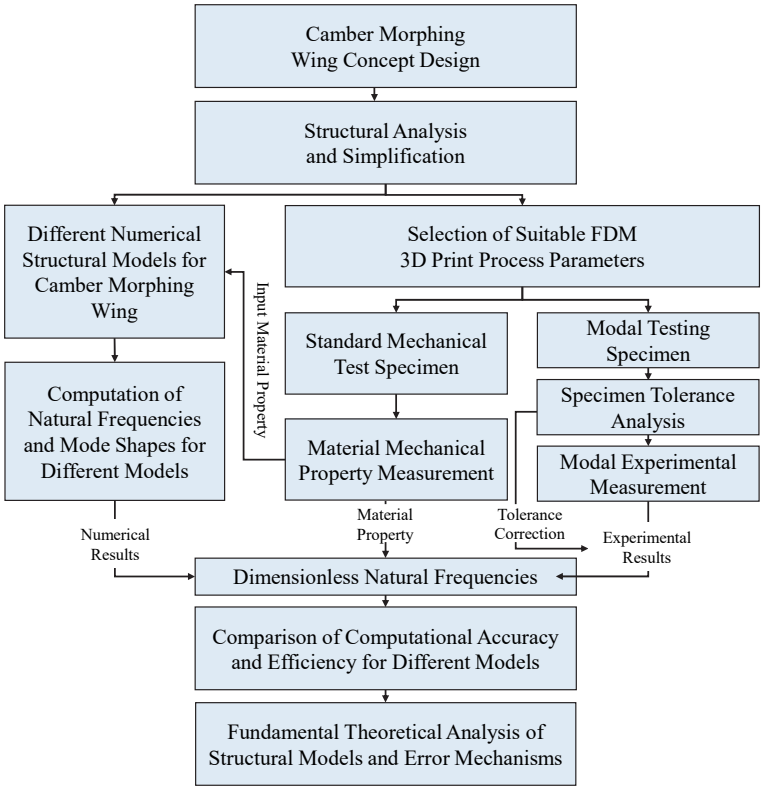

Figure 1. Flowchart of the research workflow.

2. Structural Modelling

This paper uses the Fish Bone Active Camber (FishBAC) morphing aerofoil[18] model as an example, shown in Fig. 2(a). This three-dimensional schematic represents a wing employing the FishBAC concept, where the camber morphing model consists of two airfoil segments: a stiff D-type wing spar at the front and a biomimetic flexible trailing edge at the rear. The trailing edge is fixed to the D-type wing spar, with a rigid connection. Rotating the tendon spooling pulley moves the tendons to morph the trailing edge upward or downward, producing continuous camber changes. For most camber morphing wings, the aerodynamic loads are carried primarily by a stiff wing spar, while smooth and compliant deformations of the flexible leading or/and trailing edges enable camber variation. Accordingly, the modelling approach adopted in this study is not limited to the FishBAC morphing airfoil concept used as an illustrative example.

Following the approach in [49, 51], this study neglects the non-homogeneous properties along the wing's chordwise direction and extends the 2D structural model to a 3D wing structure. The D-type spar and flexible trailing edge are simplified to rectangular beams with equal cross-sections. The spar is fixed at the fuselage, and the flexible trailing edge is fixed to the spar, simulating the real wing boundary conditions, as shown in Fig. 2(b). The spanwise direction is defined along the *y*-axis, and the chordwise

direction along the x-axis. The variables L, c, t, and f_{ef} represent spanwise, chordwise, thickness, and flexible segment ratio, respectively. The flexible segment ratio is defined as the proportion of the trailing edge length to the chordwise length. E, G, and ρ represent the material's Young's modulus, shear modulus, and density, with subscripts R and F indicating the rigid spar and flexible trailing edge, respectively. AR is the aspect ratio, also the plate's length-to-width ratio.

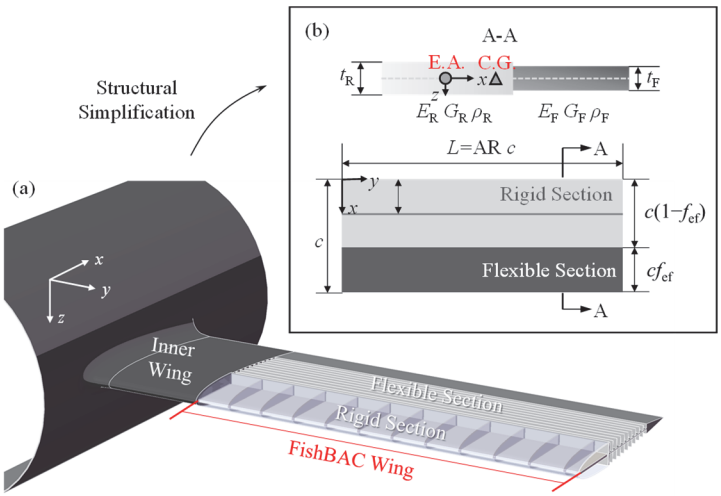

Figure 2. (a) Fish Bone Active Camber (FishBAC) morphing aerofoils. (b) Top and sectional views of a simplified structural model. (EA: Elastic Axis, CG: Centre of Gravity)

Traditional structural models for morphing wings have inherent limitations. Beam models efficiently capture spanwise deformations but fail to represent chord-wise flexibility, whereas plate models can describe chord-wise effects but inadequately capture torsional behaviour and exhibit low computational efficiency. Consequently, neither model can accurately and efficiently account for chord-wise flexibility and torsional effects simultaneously. Since the stiffness difference between the rigid and flexible sections can be at least two orders of magnitude. The rigid section is idealized as a high-AR wing, with the leading edge more susceptible to bending and torsion, for which a beam model is recommended in flutter analysis [41]. The flexible segment is simplified as a cantilever plate with a fixed support at the front boundary, attached to the rigid segment with greater stiffness. Given its low AR (much less than 4), it can be treated as a plate model. The accuracy of this approach in capturing the behaviour of a rigid-flexible coupled wing will be discussed in Section 5.3.

In finite wing theory, wings with AR less than 2, greater than 5, and between 2 and 5 are classified as small, large, and medium aspect ratio wings, respectively[54]. Table 1 summarizes the principal parameters of full-scale aircraft and scaled demonstrators equipped with camber morphing wings. The parameters include the wingspan, the equivalent semi–aspect ratio, and the flexible segment ratio. The equivalent semi–aspect ratio is defined as the aspect ratio of one cantilevered half-wing based on geometric symmetry. Accordingly, the subsequent analysis focuses on aspect ratios in the range of 3–6 and flexible segment ratios between 25% and 75%.

Table 1. The main dimensions of the verification aircraft with morphing trailing edge airfoils.

Ref	Year	Research Program	Span/m	Equivalent Semi-AR	Flexible Segment Ratio/%
[55]	1997	SARISTU Program	34.0	5.78	20
[56]	2015	VCCW Program	1.83	3.00	100
[57]	2017	Gulfstream III	22.99	6.02	20
[15]	2019	Smart Morphing Wing	1.60	2.67	25~30
[58]	2020	FishBAC Wing	1.00	3.70	24
[14]	2022	Smart-X Alpha Wing	1.80	3.60	26
[59]	2025	Time-varying Modelling	1.38	6.15	62

3. Experiment Setup

3.1 Material Test and Test Specimens Preparation

All specimens were fabricated using a Bambu X1C FDM 3D printer with Bambu PLA Basic filament (diameter 1.75 mm). Slicing was performed using Bambu Studio. The layer height and raster width were set to 0.08 mm, with a 100% infill using a "rectilinear" pattern. The nozzle diameter was 0.4 mm, the extrusion temperature was 220 °C, and the infill speed was 350 mm/s. A fine layer thickness and rectilinear infill pattern were selected to mitigate the influence of FDM build orientation on the anisotropy of the material modulus [60, 61]. As the modal analyses are conducted within the linear-elastic regime, a linear-elastic material model is appropriate for the 3D-printed specimens. Uniaxial tensile tests yielded a Young's modulus of 2.113 ± 0.105 GPa and a Poisson's ratio of 0.3. The material density is 1184 ± 4.8 kg/m³. A detailed characterization of the material mechanical properties is provided in Appendix B.2. The raw experimental data are provided in the Supplementary Materials.

FDM 3D printing is widely adopted in the fabrication of morphing wings and is therefore representative of current practice [62, 63]. To minimize the effect of manufacturing tolerance on the test structures, 25 calibration blocks were fabricated, and the tolerance verification (see Appendix B.1) confirmed consistent tolerances and sufficiently high dimensional accuracy. Figure 3(a) shows the stepped and uniform cross-section cantilever plates used in the experiments. In addition, four specimen sets were fabricated from aluminium alloy using CNC machining and served as reference specimens with isotropic and non-porous properties, as illustrated in Figure 3(b). For all test specimens, five key points were manually measured to correct the structural dimensions, thereby eliminating tolerance effects in the subsequent finite-element analyses. The exact dimensions of all specimens are provided in the Supplementary Materials.

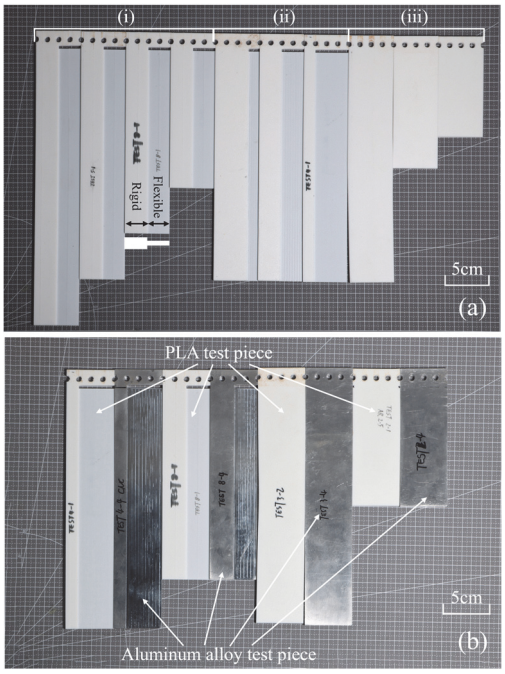

Figure 3. Experimental specimens. (a) 3D printed PLA test pieces. (i) Uniform cantilever plates with different ARs. Stepped cantilever plates with (ii) different flexible segment ratios and (iii) different ARs. (b) Aluminium alloy test pieces.

3.2 Modal Experiment Setup

The experimental setup is shown in Figs.4(a)-(c). A Polytec Scanning Vibrometer (PSV)-400 was used for linear vibration measurements[64], equipped with a PSV-I-400 MR laser head and an NI 4451 signal generation and data acquisition module. Frequency sweeps were conducted using a sound emitting periodic chirp signals in the appropriate range to match the structural response. A rectangular window function was applied, and 3200 FFT lines were used. The specific frequency range and resolution, as well as the original data of the modal test, are provided in the Supplementary Materials.

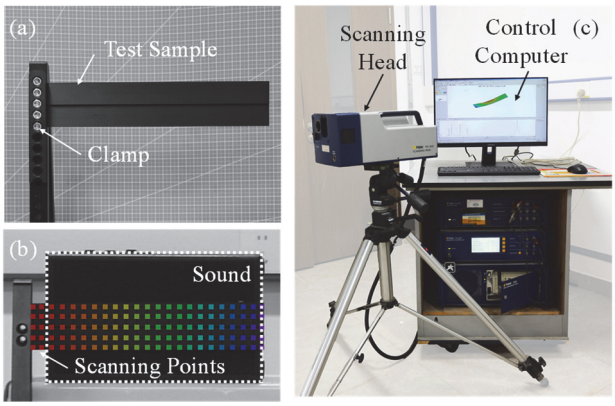

Figure 4. Non-contact modal testing setup. (a) Specimen mounting and support configuration. (b) Excitation source and scanning area. (c) Polytec PSV-400 scanning vibrometer setup.

For all specimen types, three replicates were fabricated, with both on-edge and flat build orientations to account for uncertainties introduced by the manufacturing process. The standard deviation of the

modal frequency was computed across the three specimens to mitigate the influence of manufacturing variability, material uncertainties, and measurement setup on the assessment of model accuracy.

To further verify the accuracy of the experimental protocol and minimize the effects of material anisotropy and printing defects inherent in FDM 3D printing, additional specimens with identical geometry were fabricated from CNC-machined 6061 aluminium alloy (E = 62 GPa, ν = 0.3, ρ = 2714 kg/m³), as illustrated in Fig. 3(b). The aluminium specimens serve a dual purpose: (i) to compare with previously published cantilever plate modal test data and validate the experimental setup, and (ii) to benchmark against FDM 3D printed specimens, thereby assessing the material uncertainties associated with the additive manufacturing process.

4. Finite Element Modelling and Calculation Settings

4.1 Uniform Cantilever Plate

To investigate the applicability of the plate and beam elements, which are widely used in finite element models of conventional wings, experiments were conducted using 3D-printed PLA plates with dimensions of 50 mm in width, 4 mm in thickness, and aspect ratios of 1.8, 2.5, and 5.0.

The test specimens were modelled in Abaqus/Standard 2024 using B33, B32, S8R5, S8R, and C3D8R elements, representing Euler beams (EB), shear beams (SB), thin shells (TP), thick shells (SP), and solid elements (SD), respectively. An element size of 0.5 mm was adopted to ensure mesh independence. Modal analyses were performed using the "Linear Perturbation – Frequency" step with the Lanczos eigensolver, considering the first 20 modes. Computational efficiency (CE) was evaluated based on the runtime on the two cores of an Intel i7-12700 processor.

4.2 Stepped cantilever Plate and Beam-Plate Coupled Model

To verify the accuracy of the beam-plate coupled model proposed in Section 2 for rigid-flexibly coupled structures, a stepped cantilever plate is used to simulate structures with varying stiffnesses. The computational accuracy of the plate-plate (PP), beam-plate (BP) coupled, and beam-beam (BB) models for cantilevered stepped plates is evaluated, with all element sizes and material parameters held constant. The rigid section thickness is t_R = 4mm, and the flexible section thickness is t_F =1mm.

Nastran 2020 commercial FEM software is adopted for analysing a rigid-flexible coupled stepped cantilever plate. Since previous analysis showed that shear correction has little effect on the accuracy for thin structures, the beam and plate are modelled using CBEAM and CQUAD4 elements, respectively. For the PP model, connections between plate elements of different thicknesses were realized via shared nodes, while for the BP and BB models, rigid connections between the two parts were simulated using RBAR elements, ensuring displacement compatibility at the connection nodes. Figure 5 shows the three finite element models used. Dots represent nodes, red lines and blue rectangles represent CBEAM and CQUAD4 elements, respectively, and the single point constraints (SPC) labelled

"123456" indicate that six degrees of freedom at the constrained nodes are fixed to represent the clamped end. The connection stiffness between the rigid wing spar and the flexible trailing edge was not considered; instead, a rigid connection was assumed. Shear deformations were neglected because the material is linear-elastic and the focus is on low-order natural frequencies. However, for laminated composite plates with low shear modulus or for high-frequency vibration analyses [65], shear deformation must be included to avoid significant errors. Element size is set to 0.5 mm for mesh independence. The analyses were performed using SOL 103. Extraction method was "Lanczos". The first 20 modes are considered in the FEM mode analyses. Computational efficiency is evaluated using default settings in Patran, and computational time is measured on the same computation platform in Section 4.1.

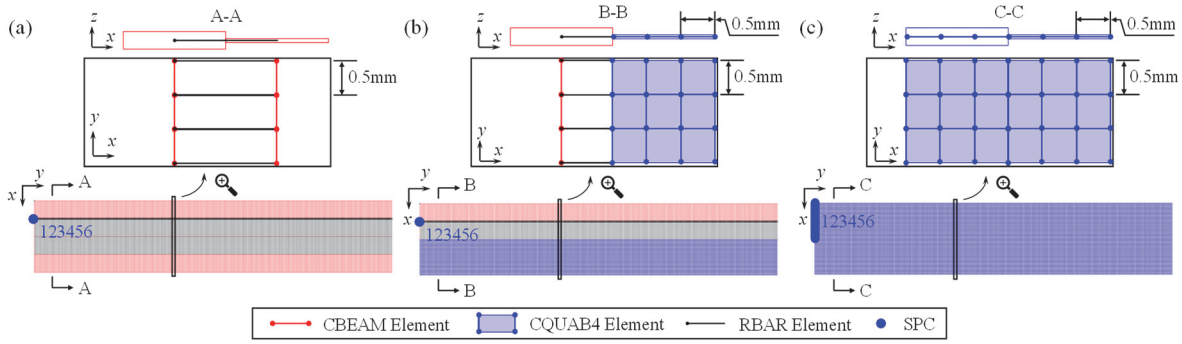

Figure 5. Finite element models. (a) Beam-Beam model. (b) Beam-Plate coupled model. (c) Plate-Plate model. Side views and local zoom-ins are shown for illustrative purposes, with mesh sizes intentionally exaggerated for clarity.

5. Experient Result and Model Comparation

5.1 Frequency Normalization

To facilitate a clear comparison between experimental and numerical results, and to enable geometry- and material-independent comparisons with other studies, the subsequent results are presented in nondimensional form [41]. For the uniform cantilever beam, assuming the length, width, and thickness are L, b, and t, respectively, the nondimensional resonance angular frequency Ω_u is defined as [41, 66, 67]:

$$\Omega_u = \omega L^2/\sqrt{\rho t/D} \tag{1}$$

In which ω is the resonance angular frequency, ρ is the material density, $D = Et^3/[12(1-\nu^2)]$ is the bending stiffness.

For the convenience of comparisons, a nondimensional angular frequency Ω_s is also adopted for the stepped cantilever plate, as commonly used in vibration studies[68], namely:

$$\Omega_s = \omega L^2/\sqrt{\rho t_R/D_R} \tag{2}$$

In which, $D_R = E_R t_R^3/[12(1-\nu_R^2)]$.

For the nondimensional analysis of the experimental results, the measured structural parameters reported in Section 3.1 were substituted into the nondimensional equations to account for manufacturing tolerances. Since the modal frequencies differ significantly across modes, a nondimensional frequency ratio λ is defined as:

$$\lambda = \frac{\Omega_{u/s}^{num}}{\Omega_{u/s}^{exp}} \tag{3}$$

which facilitates comparison between numerical(NUM) models and experiments(EXP). The subscripts u and s denote the uniform cantilever plate and the stepped plate, respectively. A value of $\lambda = 1$ indicates perfect agreement between numerical models and experiments, while deviations from unity represent modeling errors.

5.2 Uniform Cantilever Plate

Figures 6(a)-(c) show the dimensionless frequency ratios for different modes, as defined in Section 5.1, while Figs.6(d)-(f) present the bar charts of the relative error between the numerically calculated dimensionless frequencies and experimental results. Results with the same element type are color-coded for easier comparison. In Figs. 6(a)–(c), the gray dashed line represents a dimensionless frequency ratio of 1; the closer a data point lies to this line, the higher the computational accuracy of the corresponding model. Error bars on the dashed line indicate the experimental measurement uncertainties for each mode. The same presentation method is applied to all subsequent structural experimental frequencies.

Tables 2–4 summarize the experimental and numerical dimensionless natural frequencies for different aspect ratios. In these tables, EXP denotes experimental results, STD indicates the experimental uncertainty, and CNC refers to the results obtained from aluminium alloy specimens. Additionally, published experimental data are included for comparison, demonstrating the reliability of the current measurements. Table 5 summarizes the computational accuracy and efficiency of the different models, with the maximum errors in bending and torsional modal frequencies for the first five modes explicitly reported.

Analysis of all experimental results in Tables 2–4 leads to the following conclusion: comparison with published experimental results for specimens with varying geometries and materials confirms the validity of the nondimensionalization approach. The nondimensional frequencies of the 3D-printed PLA specimens, the CNC-machined aluminium specimens in this study, and previously published results show good agreement, indicating the accuracy of the experimental protocol. Moreover, the influence of anisotropy introduced by 3D printing is negligible, consistent with the material characterization results reported in Section 3.1.

Table 2. Experimental and numerical dimensionless natural frequencies of uniform plates for AR = 1.8. B = Bending mode, T = Torsion mode.

	Nondimensional Frequency $\Omega_u = \omega L^2/\sqrt{\rho t/D}$						
Mode	EB	SB	TP	SP	SD	EXP(STD)	[41]
1-B	3.28	3.28	3.43	3.43	3.41	3.41(0.04)	3.65
1-T	11.08	11.08	13.14	13.11	13.06	13.05(0.33)	15.19
2-B	20.25	20.35	21.21	21.17	21.09	21.21(0.27)	23.05
2-T	33.25	33.25	43.01	42.86	42.69	43.20(1.03)	47.99
3-B	55.42	56.16	58.55	58.29	58.09	58.83(0.72)	63.58

For the beam with a small aspect ratio (AR = 1.8), the dimensionless frequency ratios and relative error bar charts are shown in Figs. 6(a), 6(f) and Table 2. For bending modes, the beam model exhibits errors of less than 6%, whereas the plate and solid models remain within 1.5%. For torsional modes, the beam model shows errors exceeding 20%, while the plate and solid models still remain within 1.5%. This aligns with the findings in [41], where the beam model's larger error in torsional modes is attributed to neglecting the Poisson effect and the chordwise flexibility. As shown in Fig. 6(f) and Table 4, shear correction significantly improves the accuracy of the beam and plate models in predicting bending modes.

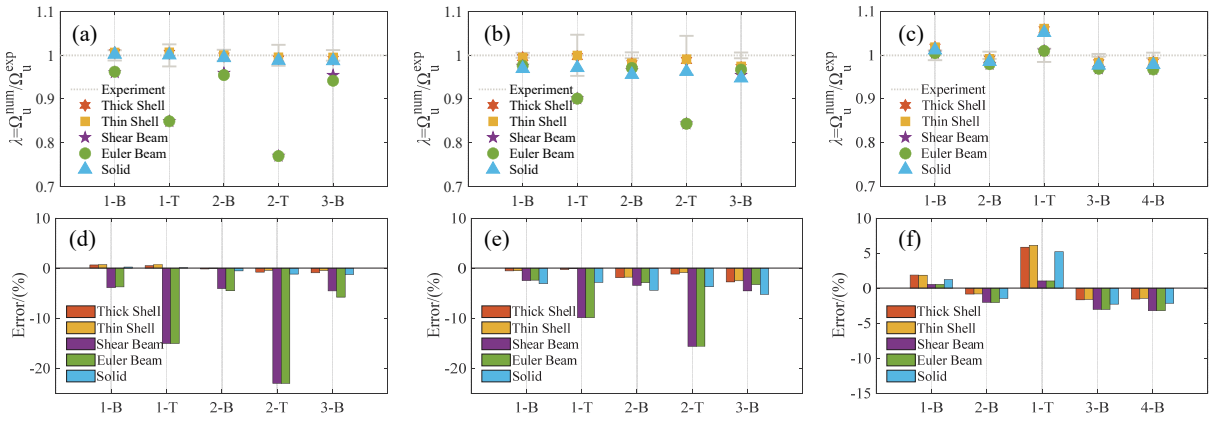

Figure 6. Comparison of experimental and numerical results. (a–c) Dimensionless frequency ratios λ(Eq.3) for different modes. The grey horizontal line at λ = 1 corresponds to the experimental reference; deviations from 1 indicate modeling error. Error bars represent experimental uncertainty. (d–f) Histograms of computational errors for different FEM models and experimental data (numbers indicate mode order; B: bending, T: torsion). The columns from left to right correspond to aspect ratios of 1.8 (a,d), 2.5 (b,e), and 5.0 (c,f), respectively.

For the medium-aspect-ratio (AR = 2.5) rectangular plate, experimental frequencies and computational errors are shown in Figs. 6(b) and 6(e). Table 3 shows detailed numerical and experimental results. The beam model is more accurate for bending frequencies but less accurate for torsional frequencies.

Table 3. Experimental and numerical dimensionless natural frequencies of uniform plates for AR = 2.5. B = Bending mode, T = Torsion mode.

	Nondimensional Frequency $\Omega_u = \omega L^2/\sqrt{\rho t/D}$									
Mode	EB	SB	TP	SP	SD	EXP(STD)	EXP(CNC)	[67]	[66]	[69]
1-B	3.43	3.42	3.49	3.49	3.40	3.51(0.02)	3.37	3.46	3.46	3.5
1-T	16.07	16.07	17.79	17.83	17.33	17.84(0.84)	18.00	17.98	17.99	17.3
2-B	21.476	21.36	21.70	21.72	21.15	22.12(0.15)	21.89	21.47	21.56	21.6
2-T	48.223	48.22	56.48	56.65	55.03	57.16(2.54)	57.07	58.48	57.46	54.8
3-B	60.135	59.35	60.46	60.60	58.93	62.18(0.41)	61.38	-	-	60.4

For the high-aspect-ratio (AR = 5) rectangular plate, the dimensionless frequency ratios and relative error bar charts are shown in Figs. 6(c) and 6(f), with the experimental and FEM results for each mode order in Fig.7. Since Abaqus cannot render the torsional deformation of beam elements (Fig. 7(a)(iii)), only the torsional displacement contours are presented. Table 4 shows detailed numerical and experimental results. For bending modes, the plate model exhibits slightly higher computational accuracy than the beam model. However, for torsional modes, the plate model shows significantly lower accuracy compared to the beam model. Since shear correction has a minimal effect, the comparison between numerical and experimental modes for the Euler beam and thin plate elements shows that models based on different theories can predict mode shapes satisfactory.

Table 4. Experimental and numerical dimensionless natural frequencies of uniform plates for AR = 5.0. B = Bending mode, T = Torsion mode.

	Nondimensional Frequency $\Omega_u = \omega L^2/\sqrt{\rho t/D}$								
Mode	EB	SB	TP	SP	SD	EXP(STD)	EXP(CNC)	[70]	[69]
1-B	3.60	3.60	3.65	3.65	3.62	3.58(0.04)	3.46	3.32	3.45
2-B	22.52	22.52	22.80	22.80	22.66	22.99(0.19)	21.76	20.84	21.1
1-T	33.76	33.76	35.46	35.37	35.16	33.42(0.51)	34.05	32.40	32
3-B	62.94	62.94	63.86	63.82	63.45	64.92(0.21)	60.83	-	59.3
4-B	122.99	122.99	125.22	125.08	124.32	127.07(0.79)	119.43	-	-

Table 5 summarizes the computational accuracy and efficiency of FEM models for uniform beams. Overall, beam models are approximately ten times more computationally efficient than plate models, while solid models are 20–30 times less efficient than beam models. In the beam and plate models, applying shear correction reduces computational efficiency. For Abaqus beam elements, considering shear reduces the system degrees of freedom (DOFs), whereas for plate elements, shear correction can increase the system DOFs. The increase in DOFs for the S8R5 element compared to the S8R element is primarily due to the use of the Discrete Kirchhoff constraint, which imposes an additional set of constraint equations to satisfy the Kirchhoff assumption [71].

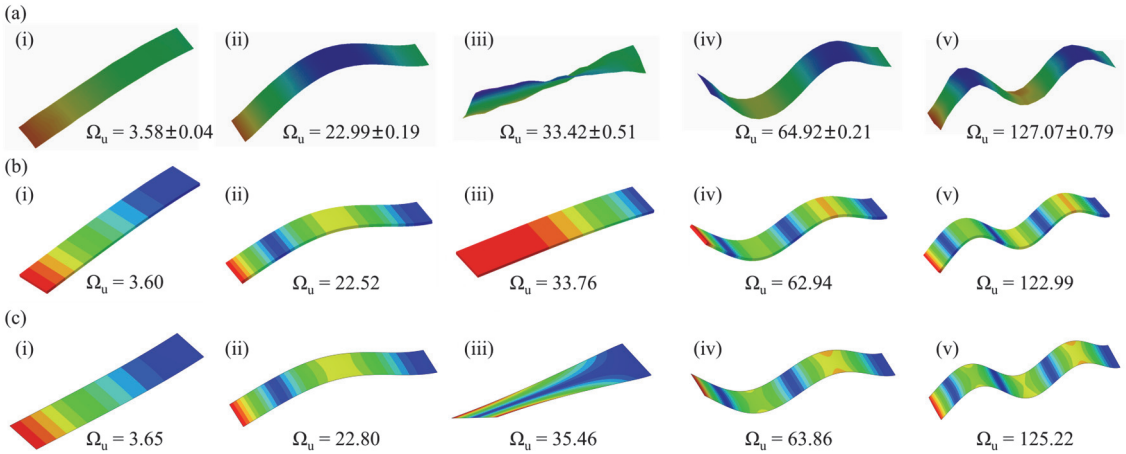

Figure 7. Comparison of experimental and numerical results for AR = 5. (a) Experimental results. (b) Euler beam model. (c) Thin plate model. (i)-(v) for 1-B, 2-B, 1-T, 3-B and 4-B modes, respectively.

Table 5. Comparison of computational accuracy and efficiency for different models of uniform plates

AR = 1.8					
Parameters	EB	SB	TP	SP	SD
DoFs	1446	2166	435366	327366	603273
CE(s)	2.2	2.8	17.7	20.5	56.1
Bend Modal Max Error (%)	5.81	2.10	0.48	0.93	1.27
Twist Modal Max Error (%)	23.04	23.04	0.44	0.81	1.20
AR = 2.5					
Parameters	EB	SB	TP	SP	SD
DoFs	2006	3006	604206	454206	836583
CE(s)	2.6	2.9	18.8	24.8	54.4
Bend Modal Max Error (%)	3.29	4.56	2.54	2.77	5.24
Twist Modal Max Error (%)	15.64	15.64	0.89	1.20	3.73
AR = 5.0					
Parameters	EB	SB	TP	SP	SD
DoFs	4004	6006	1207206	907206	16669833
CE(s)	2.8	3.2	23.5	35.6	108.5
Bend Modal Max Error (%)	3.22	3.21	1.85	1.86	2.29
Twist Modal Max Error (%)	1.03	1.03	6.11	5.85	5.20

5.3 Stepped cantilever Plate

Figures 8(a)–(c) and 8(d)–(f) present the histograms of dimensionless frequency ratios and relative errors, respectively, for cantilevered stepped plates with a fixed AR of 5 and f_{ef} of 25%, 50%, and 75%. Similarly, Figures 9(a)–(c) and 9(d)–(f) show the corresponding histograms for plates with a fixed f_{ef} of 50% and ARs of 3, 4, and 6. For comparison, Tables 6 and 7 present the detailed results corresponding to Figs. 8 and 9, alongside experimental data from aluminum alloy specimens. The comparison confirms that a linear-elastic isotropic model is appropriate for the 3D-printed specimens. Computational

accuracy and efficiency are summarized in Table 8, which explicitly reports the maximum errors in bending and torsional frequencies for the first six modes.

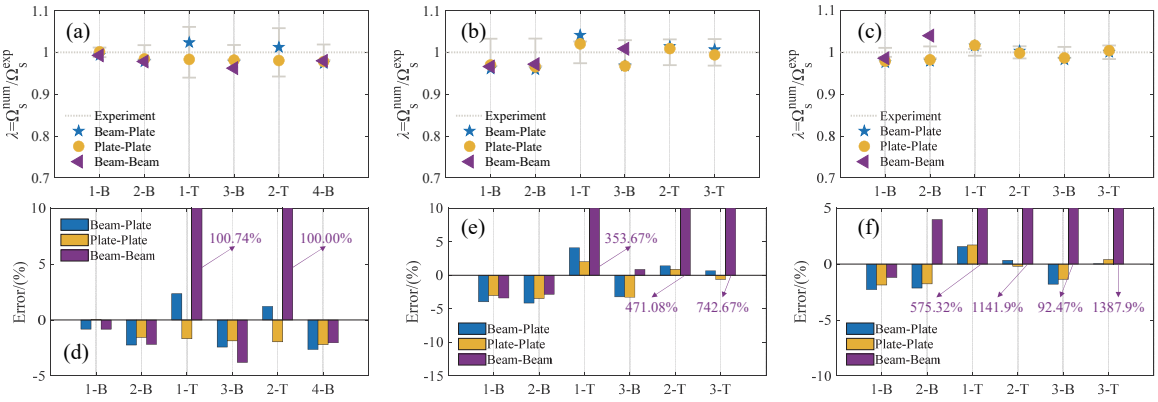

Figure 8. Comparison of experimental and numerical results for a stepped plate with AR = 5 and varying flexible segment ratios. (a–c) Dimensionless frequency ratios λ (Eq.3) for different modes. The grey horizontal line at λ = 1 corresponds to the experimental reference; deviations from 1 indicate modeling error. Error bars represent experimental uncertainty. (d–f) Relative error histograms comparing FEM models with experimental results, corresponding to flexible segment ratios of 25% (a,d), 50% (b,e), and 75% (c,f), from left to right.

In Fig. 8, the errors for the torsional modes of the BB model are excessively large, and are explicitly indicated in the figure. A comparison of experimental mode shapes with FEM results for a cantilevered stepped plate (AR = 5, f_{ef} = 75%) is shown in Fig. 9, due to the weak mode calculation capability of the BB model, as shown in Table 5, the mode shapes are not shown here. Fig. 11 shows the modal assurance criteria (MAC) computed using mode shapes as identified from experimental mode shapes and those computed from numerical models as shown in Fig.10. The MAC is normally used to quantify the congruence between two different mode shapes [72]. Both the BP coupled and PP models can calculate reasonable mode shapes, but accuracy and computational efficiency must be considered.

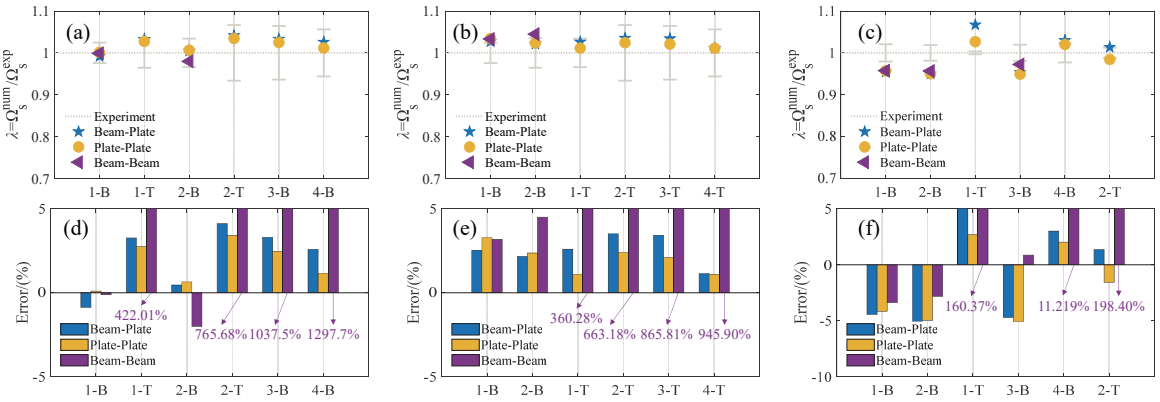

Figure 9. Comparison between experimental and numerical results. (a–c) Dimensionless frequency ratios λ(Eq.3) for different modes. The grey horizontal line at λ = 1 corresponds to the experimental reference; deviations from 1 indicate modeling error. Error bars represent experimental uncertainty. (d)–(f) Histograms of computational

errors for different FEM models relative to experimental results (numbers indicate corresponding mode orders, B: Bending, T: Torsion). Columns from left to right correspond to AR = 3 (a,d), 4 (b,e), and 6 (c,f), respectively.

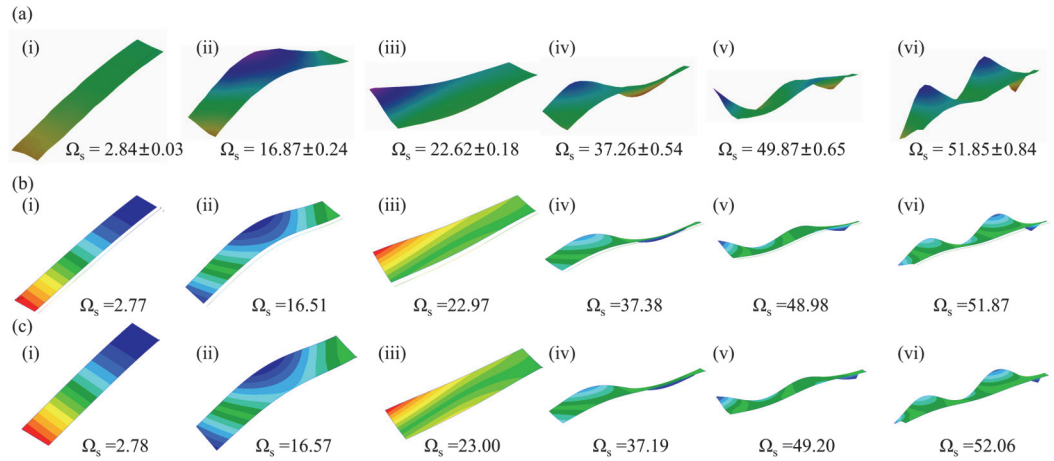

Figure 10. Comparison of experimental and numerical results for a stepped cantilever plate with AR = 5 and f_{ef} = 75% (a) Experimental results (b) Beam-Plate coupled model (c) Plate-Plate model. (i)-(vi) are for modes 1-B, 2-B, 1-T, 2-T, 3-B and 3-T, respectively.

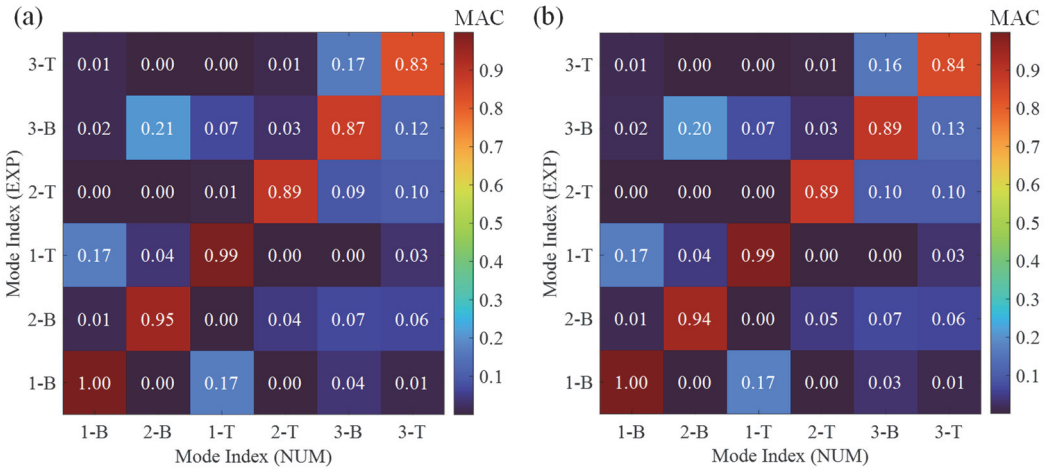

Figure 11. MAC between test mode shapes and FEA mode shapes for a stepped cantilever plate with AR = 5 and f_{ef} = 75%. (a) Beam-plate coupled model, (b) Plate-plate model.

To evaluate model performance under different aspect ratios, Figs. 8(b), 8(e), and 9 show that the BP coupled model achieves good accuracy for both bending and torsional modes. The PP model provides the highest accuracy among the three models. The BB model performs well for low-order bending modes but exhibits large errors in torsional modes. Figure 12 compares experimental mode shapes with FEM results for a cantilevered stepped plate (AR = 3, f_{ef} = 50%). BB model's mode shapes are omitted due to poor torsional predictions, as shown in Table 6. Fig. 13 shows the modal assurance criteria (MAC) computed using mode shapes as identified from experimental mode shapes and those computed from numerical models as shown in Fig.12. Both BP coupled and PP models match the experiments well.

The accuracy generally falls within experimental uncertainty. Table 8 shows computational efficiency. The BP coupled model is roughly twice as fast as the PP model while maintaining similar accuracy. This efficiency gain comes from using beam elements to reduce the number of plate elements.

Table 6. Experimental and numerical dimensionless natural frequencies of stepped plates for AR = 5.0 and different f_{ef}.

		Nondimensional Frequency $\Omega_s = \omega L^2/\sqrt{\rho t_R/D_R}$				
f_{ef}	Mode	BB	BP	PP	EXP(STD)	EXP(CNC)
25%	1-B	3.47	3.48	3.51	3.50(0.04)	
	2-B	21.75	21.74	21.89	22.24(0.38)	
	1-T	79.57	40.57	38.97	39.64(2.40)	
	3-B	59.85	60.70	61.04	62.20(1.10)	
	2-T	238.71	120.81	117.02	119.35(6.87)	
	4-B	118.95	118.21	118.76	121.42(2.25)	
50%	1-B	3.27	3.25	3.29	3.38(0.11)	
	2-B	20.45	20.17	20.31	21.04(0.69)	
	1-T	153.59	35.24	29.62	33.85(0.88)	
	3-B	57.18	54.87	54.83	56.69(1.65)	
	2-T	460.80	81.83	81.41	80.69(2.48)	
	3-T	767.97	91.74	90.59	91.14(2.90)	
75%	1-B	2.80	2.77	2.78	2.84(0.03)	2.70
	2-B	17.54	16.51	16.57	16.87(0.24)	16.08
	1-T	152.75	22.97	23.00	22.62(0.18)	21.77
	2-T	462.71	37.38	37.19	37.26(0.54)	34.62
	3-B	95.98	48.98	49.20	49.87(0.65)	47.39
	3-T	771.55	51.87	52.06	51.85(0.84)	49.99

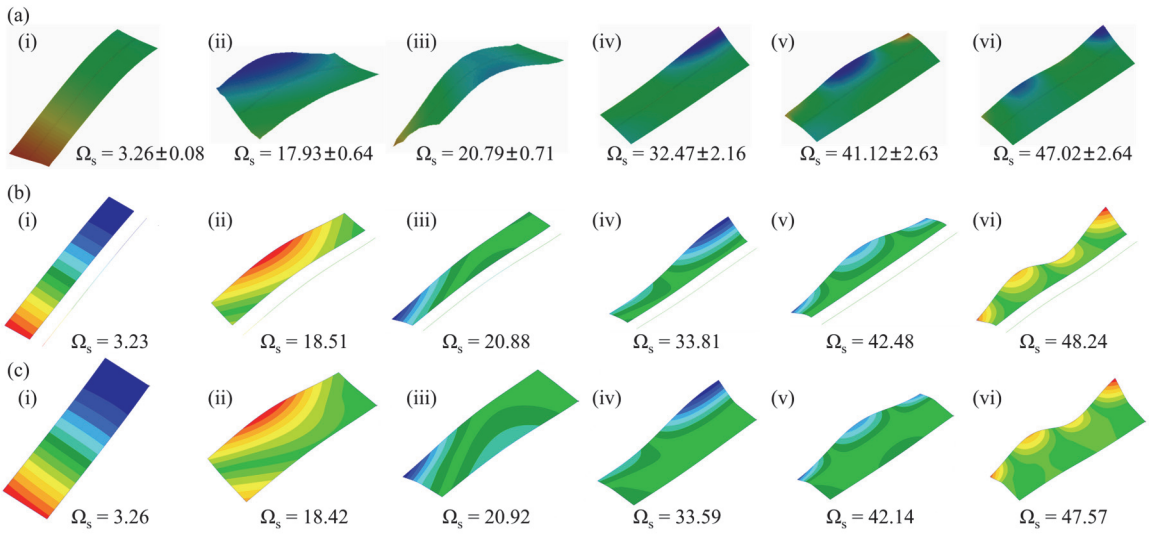

Figure 12. Comparison of experimental and numerical results for a stepped cantilever plate with AR = 3 and f_{ef} = 50% (a) Experimental results (b) Beam-Plate coupled model (c) Plate-Plate model. (i)-(vi) are for modes 1-B, 1-T, 2-B, 2-T, 3-T and 4-T, respectively.

Table 7. Experimental and numerical dimensionless natural frequencies of stepped plates for f_{ef} = 50% and different AR.

AR	Mode	Nondimensional Frequency $\Omega_s = \omega L^2/\sqrt{\rho t_R/D_R}$				
		BB	BP	PP	EXP(STD)	EXP(CNC)
3	1-B	3.26	3.23	3.26	3.26(0.08)	
	1-T	93.59	18.51	18.42	17.93(0.64)	
	2-B	20.37	20.88	20.92	20.79(0.71)	
	2-T	281.13	33.81	33.59	32.47(2.16)	
	3-B	467.77	42.48	42.14	41.12(2.63)	
	4-B	657.18	48.24	47.57	47.02(2.64)	
4	1-B	3.26	3.24	3.27	3.16(0.06)	3.13
	2-B	20.44	19.98	20.02	19.56(0.36)	19.27
	1-T	124.10	27.66	27.26	26.96(0.57)	27.24
	2-T	371.77	50.43	49.89	48.71(0.96)	48.64
	3-T	620.04	66.40	65.54	64.20(1.19)	66.22
	4-T	870.10	84.14	84.11	83.19(1.30)	84.70
6	1-B	3.26	3.25	3.26	3.41(0.07)	
	2-B	20.40	20.29	20.31	21.37(0.40)	
	1-T	105.34	43.17	41.54	40.46(0.14)	
	3-B	57.02	56.04	55.82	58.80(1.15)	
	4-B	111.73	103.49	102.49	100.46(2.31)	
	2-T	316.97	107.66	104.56	106.22(1.28)	

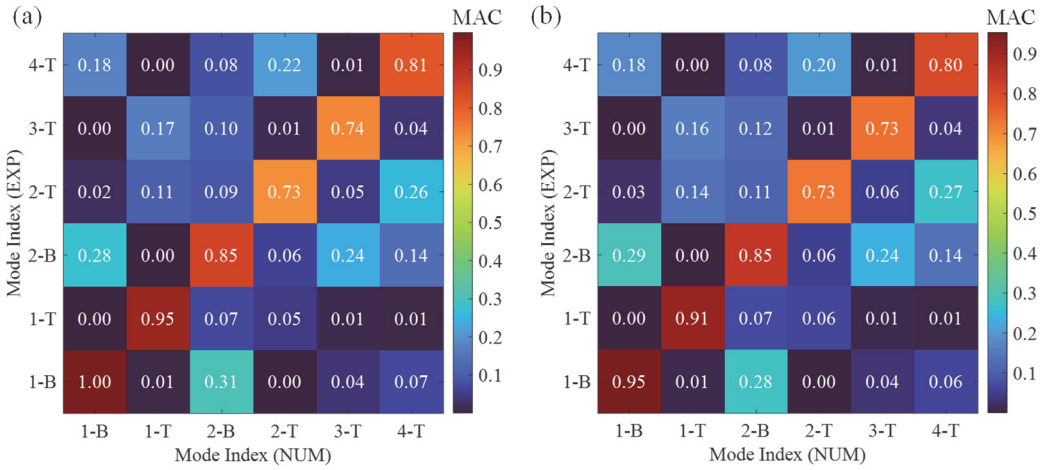

Figure 13. MAC between test mode shapes and FEA mode shapes for a stepped cantilever plate with AR = 3 and f_{ef} = 50%. (a) Beam-plate coupled model, (b) Plate-plate model.

Table 8. Comparison of computational accuracy and efficiency for different models of stepped plates.

Model	AR = 5 f_{ef} = 25%			AR = 3 f_{ef} = 50%		
Parameters	BB	BP	PP	BB	BP	PP
DoFs	6012	78156	143239	3612	92112	180600
CE(s)	0.2	2.6	10.4	0.1	3.5	6.2
Bend Modal Max Error (%)	3.76	2.64	2.20	1298	2.53	3.29
Twist Modal Max Error (%)	100.0	2.35	1.95	765.7	3.52	2.41
Model	AR = 5 f_{ef} = 50%			AR = 4 f_{ef} = 50%		
Parameters	BB	BP	PP	BB	BP	PP
DoFs	6012	153306	300600	4812	122712	240600
CE(s)	0.2	5.0	10.1	0.2	4.3	7.8
Bend Modal Max Error (%)	3.39	4.14	3.46	4.50	3.29	2.53
Twist Modal Max Error (%)	742.7	4.10	2.01	945.9	1.10	3.52
Model	AR = 5 f_{ef} = 75%			AR = 6 f_{ef} = 50%		
Parameters	BB	BP	PP	BB	BP	PP
DoFs	6012	231462	300600	7212	183906	360600
CE(s)	0.2	5.5	7.5	0.3	5.8	10.4
Bend Modal Max Error (%)	92.47	2.29	1.88	4.58	5.05	5.08
Twist Modal Max Error (%)	1141	1.57	1.71	160.4	6.71	2.68

6. Comparative Analysis

6.1 Main Disagreement Between Classical Beam and Plate Theories

Appendix A presents the fundamental theories and simplifying assumptions of classical beam and plate theories. In the plate theory, the bending and torsional displacement fields from beam theory are substituted into the plate formulation, enabling a formal comparison by examining the dynamic equations of uniform, constant-section beams. By comparing Eqs. (A.2) and (A.3) with Eqs. (A.12) and (A.17), it can be seen that:

$$Db = \frac{Et^3 b}{12(1-\nu^2)} = \frac{EI}{1-\nu^2} > EI \tag{4}$$

$$2Db(1-\nu) = \frac{Et^3 b}{2(1+\nu)} = G\frac{t^3 b}{3} > GJ \tag{5}$$

$$\rho I_z = \rho \frac{b^3 t}{12} < \rho \frac{b t^3}{12}\left(1 + \frac{b^2}{t^2}\right) = \rho I_0 \tag{6}$$

The discrepancy in Eq. (4) arises from the Poisson effect neglected in beam theory. The difference in Eq. (5) stems from plate theory's inability to account for warping during torsion of a non-circular cross-section, while the difference in Eq. (6) results from the distinct displacement assumptions adopted for torsional deformation in beam and plate theory. Overall, plate theory tends to overestimate stiffness for both bending and torsional modes. For thin plates($t/b \ll 1$), the inequalities in Eqs. (5) and (6) become approximately equal. In general, plate theory predicts higher bending and torsional stiffness than beam theory, whereas the polar moment of inertia calculated from plate theory is smaller than that from beam theory.

For bending modes, all numerical results in this study indicate that the plate model predicts higher bending frequencies than the beam model, owing to the inclusion of the Poisson effect in plate theory. In addition, the PP model yields slightly higher bending frequencies than the BP coupled model. For torsional modes, the beam model predicts lower torsional frequencies than the plate model. As the AR increases, the beam model provides more accurate torsional predictions. For a constant AR, an increase in f_{ef} reduces the difference in torsional frequency between the PP and BP models. This occurs because a larger flexible segment causes the terms in Eqs. (5) and (6) to become nearly equal. As the AR increases, the beam model becomes more accurate in predicting torsional frequencies. For high ARs, warping correction is therefore important. Plate theory neglects torsional warping, causing significant errors in torsional mode predictions.

For small ARs, the beam model's error can exceed 15%, rendering it unreliable. Eqs. (A.1) and (A.7) show that the neutral-plane deformation in plate theory accounts for curvature variations in both the x and y directions. For small ARs, chordwise and spanwise stress levels are comparable [40], and chordwise curvature must be considered in modal analysis. Similarly, for camber morphing wings, the chordwise curvature of the flexible trailing edge and spanwise bending deformations are key dynamic contributors, justifying the use of plate theory for modelling the flexible trailing edge. For the rigid leading edge, which has a larger AR and undergoes primarily bending and torsion, a beam model with fewer degrees of freedom is sufficient to accurately capture the structural response.

6.2 Coupled Model Theoretical Analysis

Both experimental and numerical models indicate that the beam-beam coupled model achieves high accuracy in analysing bending modes, but introduces significant errors in the prediction of torsional modes. To further investigate the impact of the rigid section assumption in beam theory on the dynamic characteristics, this section simplifies the analysis using beam theory. The stepped cantilever beam used in the study can be approximated as a uniform cantilever beam with a flexible plate fixed at its rear end. For this simplified analysis, the response of the flexible plate is neglected.

When using the beam-beam coupled model, as shown in Fig.7(a), the analysis assumes that all chordwise bending is neglected, and the system is treated as an eccentric beam system where the elastic axis does not coincide with the centre of mass, as shown in Fig.2(b). Further simplification assumes no discrepancy between the elastic axis and the centre of mass. In this case, the bending stiffness EI_{BB}, torsional stiffness GJ_{BB}, unit mass ρA_{BB}, and unit rotational inertia $\rho I_{0,\mathrm{BB}}$ for the simplified beam-beam coupled model are given by the following expressions

$$EI_{\mathrm{BB}} = E_{\mathrm{F}}I_{\mathrm{F}} + E_{\mathrm{R}}I_{\mathrm{R}} \tag{7}$$

$$GJ_{\mathrm{BB}} = G_{\mathrm{F}}J_{\mathrm{F}} + G_{\mathrm{R}}\left[J_{\mathrm{R}} + \left(\frac{c}{2}\right)^2 b_{\mathrm{R}}t_{\mathrm{R}}\right] \tag{8}$$

$$\rho A_{\mathrm{BB}} = \rho_{\mathrm{F}} b_{\mathrm{F}} t_{\mathrm{F}} + \rho_{\mathrm{R}} b_{\mathrm{R}} t_{\mathrm{R}} = m_{\mathrm{F}} + m_{\mathrm{R}} \tag{9}$$

$$\rho I_{0,\mathrm{BB}} = \rho_{\mathrm{R}} I_{0,\mathrm{R}} + \rho_{\mathrm{F}} I_{0,\mathrm{F}} + \rho A_{\mathrm{BB}} x_\alpha^2 + m_{\mathrm{R}} x_\alpha^2 + m_{\mathrm{F}}\left(\frac{c}{2} - x_\alpha\right)^2 \tag{10}$$

x_α represents the distance between the elastic axis and the center of mass, expressed as

$$x_\alpha = \frac{c}{2}\frac{f_{\mathrm{ef}} t_{\mathrm{F}} \rho_{\mathrm{F}}}{(1 - f_{\mathrm{ef}}) t_R \rho_{\mathrm{R}} + f_{\mathrm{ef}} t_{\mathrm{F}} \rho_{\mathrm{F}}} \tag{11}$$

For the plate-beam coupled model, the same simplification method is applied. Since the plate model does not require the rigid section assumption, the contribution of the flexible trailing edge to the torsional stiffness can be neglected. However, because the distance between trailing edge to the elastic axis is significant, its contribution to the mass and rotational inertia cannot be ignored. Therefore, the corresponding stiffness and inertial parameters in the simplified plate-plate coupled model are given by

$$EI_{\mathrm{BP}} = E_{\mathrm{F}}I_{\mathrm{F}} \tag{12}$$

$$GJ_{\mathrm{BP}} = G_{\mathrm{R}}J_{\mathrm{R}} \tag{13}$$

$$\rho A_{\mathrm{BP}} = \rho A_{\mathrm{BB}} \tag{14}$$

$$\rho I_{0,\mathrm{BP}} = \rho I_{0,\mathrm{BB}} \tag{15}$$

By substituting Eqs.(7)-(15) into Eqs.(A.7)-(A.8), the natural frequencies for the simplified plate-plate coupled model (SBB) and the plate-beam coupled model (SBP) can be derived.

For example, by selecting a stepped cantilever beam with AR = 5 and f_{ef} = 75% (Fig.9), and another stepped cantilever beam with AR = 3 and f_{ef} = 50% (Fig.12), the analytical results are compared with the first bending and torsional natural frequencies obtained from the numerical beam-beam coupled and plate-beam coupled models, as presented in Table 9.

It can be observed that by simply neglecting the right-hand term in Eq.(7) due to the rigid section assumption, i.e., the enhancement of torsional stiffness by the flexible segment, a closer match to the experimental results for the torsional frequency can be achieved. The bending frequencies, however, do not show significant differences between the models, as the underlying physics remains unchanged. Although the model has undergone considerable simplification, the reduced model still reflects the fundamental differences between the two original models. Significant discrepancies in torsional mode predictions can result in considerable errors in flutter analysis [41], potentially undermining the reliability of the aeroelastic results. Therefore, careful selection of an appropriate structural model is essential, with its suitability assessed according to the specific application and performance requirements.

Table 9. Comparison of model frequencies between simplified models, numerical models, and experimental results

f_{ef} = 75% AR = 5	Frequency/Hz				
Mode	SBP	NBP	SBB	NBB	EXP
1-B	13.1	11.4	13.1	11.4	13.5
1-T	113.0	94.3	798.8	513.8	101
f_{ef} = 50% AR = 3	Frequency/Hz				
Mode	SBP	NBP	SBB	NBB	EXP
1-B	38.79	36.9	38.79	37.0	42
1-T	210.1	211.5	854.9	959.0	223

Table 10. Model selection guidelines for cantilever and stepped plates

Plate	Parameters	Recommended Model	Error Range	Efficiency	Application
Uniform	AR > 5	Beam	Bending < 4% Torsion < 2%	High	Preliminary design
	AR < 4	Plate	All modes < 2%	Medium	Flutter prediction
Stepped	AR∈[3,6] f_{ef} ∈[25,75]%	Beam-Plate	Bending < 5.1% Torsion < 6.7%	Medium	Preliminary design
		Beam-Beam	Bending < 4% Torsion > 100%	High	Only for low order bending modes
		Plate-Plate	All modes < 3.5%	Low	Flutter prediction

6.3 Model Selection Guidelines

Based on our analysis method and results, Table 10 summarizes the recommended models for different structural configurations and applications, using the 10% frequency error threshold [72] as the acceptance criterion. Table 10 shows that, for any plate configuration, the plate model provides the

highest accuracy. This level of accuracy (error < 5%) satisfies the requirements for aeroelastic analysis [32]. Therefore, the pure plate model can be used when higher accuracy is required. However, for scenarios that involve extensive computations, such as structural optimization and parametric analysis, the plate–beam coupled model is preferred. Although its accuracy is slightly lower, it offers higher computational efficiency. This advantage remains even though the coupled model is more complex to build.

7. Discussion

7.1 Limitations of Current Beam-Plate Coupled Model

This study demonstrates, through theoretical, numerical, and experimental investigations, that the beam–plate coupled model offers advantages in both computational accuracy and efficiency. However, several limitations of the current model should be noted.

First, all materials used in this study are linear-elastic. In practice, morphing aircraft widely employ hyperelastic or viscoelastic polymers [73] and anisotropic lightweight carbon-fibre-based composite materials [74]. Furthermore, under preload conditions or camber-driven actuation, morphing wings may undergo large deformations, in which case both material and geometric nonlinearities become significant and cannot be neglected [47]. The effects of material and structural damping are not explicitly incorporated in the present linear modal analysis.

Second, the present models are relatively simple and do not fully capture the complex structural features of morphing wings. It remains to be assessed whether the rigid leading edge can be accurately represented by a statically condensed beam [35], the flexible trailing edge by an equivalent varying inertial and stiffness plate [25], and whether the connection stiffness between the leading and trailing edges can be properly modeled. The model's ability to handle complex, discontinuous stiffness distributions and structural anisotropy also requires further investigation [58].

Finally, the present study considers the main dimensions range of the verification aircraft with morphing trailing edge airfoils. More general wing geometries encountered in practice—such as those involving sweep angle and taper ratio—have not been addressed. In addition, the applicability of the current model to configurations with very high or very low aspect ratios remains to be systematically verified.

7.2 Future Directions

Future work includes applying the BP coupled model to aeroelastic or fluid–structure interaction analyses to evaluate its effectiveness in capturing the coupling between structural response and aerodynamic loads. Furthermore, aeroelastic models based on the BP coupled approach can be integrated into multidisciplinary design optimization frameworks for camber morphing wings under aeroelastic constraints [38].

For morphing wings with large ARs and high flexibility, a BP coupled model incorporating large-deformation and material anisotropy assumptions is needed to analyze nonlinear structural dynamics and nonlinear aeroelastic responses. Rigid-body degrees of freedom can also be included to establish a rigid–flexible coupled flight dynamics model [8] and develop real-time aeroelastic control systems [22].

Experimental studies on actual wing structures are required to evaluate whether the BP coupled model maintains consistent accuracy when handling nonuniform stiffness and mass distributions. Further investigations should consider the structural response under preload and time-varying morphing trailing edge, assessing whether the model can capture time-dependent stiffness and inertia variations and predict the time-dependent aeroelastic stability of camber morphing wings [59].

8. Conclusions

This study investigated the modal characteristics of uniform and stepped cantilever plates representing simplified active camber morphing wing structures. Under the assumptions of linear small-amplitude vibrations and isotropic material behavior, and within the main dimensions range of the verification aircraft with morphing trailing edge airfoils, the following conclusions can be drawn:

1. For a uniform cantilever plate with an aspect ratio > 4, the beam element in the FEM model closely matches experimental values. For aspect ratios < 4, the plate element is preferred. Beam models are approximately ten times more computationally efficient than plate models, while solid models are 20–30 times less efficient than beam models.

2. Both the plate-plate and plate-beam coupled models predict modal shapes with some accuracy. The plate-beam coupled model is the most efficient for stepped cantilever plates, offering a satisfactory accuracy. The beam–plate model is roughly twice as fast as the plate–plate model while maintaining similar accuracy. This model remains applicable for rigid–flexible coupled structures and can be extended to other morphing wings.

3. The primary source of discrepancies among the models arises from the simplifying assumptions in the beam and plate theories. Compared to the beam model, the plate model overestimates both bending and torsional stiffness, leading to higher predicted structural frequencies. The beam-beam model works well for low order bending modes but introduces large errors in torsional modes due to the rigid section assumption.

Acknowledgments

This project has received funding from National Natural Science Foundation of China (Grant No. 92271104, 12102017) and Beijing Natural Science Foundation (Grant No. 1232014).

Appendix A Theoretical Background

A.1 The Beam Theory

In aeroelastic analyses, the Euler–Bernoulli beam theory and Saint–Venant torsion theorem [40] are commonly used to derive heave and torsion dynamic equations. The main difference between beam and plate theories lies in the allowed displacement fields. Beam theory typically describes slender structures using the deformation of the neutral axis and out-of-plane deformation of the cross-section. In Euler–Bernoulli beam theory, it is assumed that cross-sections remain perpendicular to the neutral axis and retain their rigidity during deformation.

For a uniform cantilever beam, let the beam length, width, and thickness be L, b, and t, aligned with the x-, y-, and z-axes, respectively, with the origin at the intersection of the neutral axis and the fixed end. Let the transverse deflection and torsional rotation of the neutral axis be $W(x)$ and $\Psi(x)$. The displacement of an arbitrary point on the beam along the three axes, u_x, u_y and u_z, can then be expressed as

$$u_x = -z\frac{\partial W(x)}{\partial x}, u_y = -z\Psi(x), u_z = W(x) + y\Psi(x) \tag{A.1}$$

Since the cross-section undergoes rigid-body rotation, the displacement field above does not account for sectional deformation. The primary resonance dynamic equation in the frequency domain for a Euler beam and a torsional beam is given by [40]

$$EI\frac{d^4W}{dy^4} - \rho S_0\omega^2\Psi - \rho A\omega^2 W = 0 \tag{A.2}$$

$$GJ\frac{d^2\Psi}{dy^2} - \rho S_0\omega^2 W - \rho I_0\omega^2\Psi = 0 \tag{A.3}$$

In which A, I, and J are the cross-sectional area, the second moment of area about the natural axis, and the polar moment of inertia, respectively, and ρS_0 and ρI_0 are the unbalanced mass and rotational inertia of the unit length about the center of twist. For a rectangular cross-section ($\rho S_0 = 0$), the expressions are given by [40]

$$I = \frac{bt^3}{12} \tag{A.4}$$

$$J = \frac{bt^3}{3}\left(1 - \frac{192t}{\pi^5 b}\sum_{n=1,3,\ldots}^{\infty}\frac{1}{n^5}\tanh\frac{n\pi b}{2t}\right) \approx \frac{bt^3}{3}\left(\frac{t}{b} \ll 1\right) \tag{A.5}$$

$$I_0 = \frac{bt^3}{12}\left(1 + \frac{b^2}{t^2}\right) \tag{A.6}$$

From the dynamic equations, the i-th order bending natural frequency ω_{B}^{i} and torsional natural frequency ω_{T}^{i} can be expressed as follows

$$\omega_{\mathrm{B}}^{i} = k_i^2 \sqrt{\frac{EI}{\rho A L^4}} \quad (i = 1,2,3 \dots) \tag{A.7}$$

$$\omega_{\mathrm{T}}^{i} = \frac{(2i-1)\pi}{2L} \sqrt{\frac{GJ}{\rho I_0}} \quad (i = 1,2,3 \dots) \tag{A.8}$$

In which k_i is a constant dependent only on the boundary conditions, where $k_i = \{1.8751, 4.6941, 7.8548, 10.9955, 14.1372, \dots\}$.

According to the generalized Hooke's law, the presence of the Poisson effect causes a structure subjected to normal stress in any direction to experience normal strains in all directions. For a beam under bending, axial normal stresses induce not only axial strains but also lateral strains, which theoretically alter the beam's thickness and width. The assumption of a rigid cross-section in beam theory, however, prevents such sectional deformation after bending.

A.2 The Plate Theory

Plate theory describes the deformation of flat structures by superimposing the displacement of the mid-surface and the deformation of the cross-section. The Kirchhoff plate theory, the most widely used plate theory, neglects shear deformation and assumes that cross-sections remain planar and perpendicular to the mid-surface before and after deformation. The coordinate system is defined consistently with Section 4.1. Considering only the mid-surface displacement along the z-axis, $\overline{W}(x, y)$, the displacement field at any point in the plate can be expressed as

$$u_x = -z\frac{\partial \overline{W}(x,y)}{\partial x}, u_y = -z\frac{\partial \overline{W}(x,y)}{\partial y}, u_z = \overline{W} \tag{A.9}$$

The primary resonance dynamic equation in the frequency domain for a Kirchhoff plate is given by

$$D\left(\frac{\partial^4 \overline{W}}{\partial x^4} + 2\frac{\partial^4 \overline{W}}{\partial x^2 \partial y^2} + \frac{\partial^4 \overline{W}}{\partial y^4}\right) - \rho t \omega^2 \overline{W} = 0 \tag{A.10}$$

To compare plate theory with beam theory, torsional deformation in the plate is neglected, and $\overline{W}$ is assumed to have the same form as the bending displacement u_z in Eq. (A.1)

$$\overline{W}(x, y) = W(x) \tag{A.11}$$

Substituting Eq. (A.9) into Eq. (A.8) and multiplying by the plate width yields

$$Db\frac{\partial^4 W}{\partial x^4} - \rho AW\omega^2 = 0 \tag{A.12}$$

For torsional deformation, the governing equation can be derived from the internal force equilibrium based on plate theory. Assuming the plate undergoes pure torsion, $\bar{W}$ is taken to have the same form as the torsional displacement u_z in Eq. (A.1)

$$\bar{W}(x,y) = y\Psi(x) \tag{A.13}$$

Based on the expression for the torsional moment M_{xy} in plate theory, substitution of Eq. (A.12) yields

$$M_{xy} = -D(1-\nu)\frac{\partial^2 w}{\partial x \partial y} = -D(1-\nu)\frac{\partial \Psi}{\partial y} \tag{A.14}$$

Hence, the total torsional moment of the section, T, is expressed as

$$T = \int_{-b/2}^{b/2} M_{xy}dx = -D(1-\nu)b\frac{\partial \Psi}{\partial y} \tag{A.15}$$

During torsional deformation, the distributed torque is contributed by the inertia terms

$$q = \int_{-b/2}^{b/2} y\left(-\rho hy\frac{\partial^2 \Psi}{\partial t^2}\right)dy = -\rho\frac{b^3 h}{12}\frac{\partial^2 \Psi}{\partial t^2} = -\rho I_z\frac{\partial^2 \Psi}{\partial t^2} \tag{A.16}$$

Torsional equilibrium yields the following equation

$$2Db(1-\nu)\frac{\partial^2 \Psi}{\partial y^2} - \rho I_z\frac{\partial^2 \Psi}{\partial t^2} = 0 \tag{A.17}$$

Appendix B Characterization of the 3D-printed specimens

B.1 Dimensional accuracy

The dimensional accuracy of the 3D printer was evaluated to account for manufacturing tolerances in the experimental results. Twenty-five calibration cubes (20 mm edge length) were printed and measured at three locations each using a micrometer (resolution: 0.001 mm). The mean measured deviation (and standard deviation) was 0.016 mm (0.028 mm) on the X-axis, 0.056 mm (0.029 mm) on the Y-axis, and 0.020 mm (0.015 mm) on the Z-axis. All deviations were within 0.06 mm, demonstrating higher precision on the X and Z axes than on the Y axis, and greater consistency in the X–Y plane than along the Z axis.

B.2 Mechanical properties

Standard mass blocks were printed, and their volume and mass were measured using a micrometer and electronic balance. The density of the material, calculated using the mass and volume of standard square

samples (10mm×10mm×10mm) prepared under the same manufacturing conditions, was found to be 1184±4.8kg/m³. Regarding potential air gaps or porosity in the 3D-printed PLA test pieces, a comparison with the nominal filament density indicated a true infill ratio of 97.16%. In general, relative density was higher than 90% suggesting a quite low amount of internal defects [60].

As shown in Fig. B1, to analyze anisotropy associated with the FDM process, specimens were printed along four build orientations: the X-axis, Y-axis, 45° to the -Y-axis, and Z-axis (upright). For the X-axis, Y-axis, and 45° orientations, specimens were fabricated with the thickness direction either perpendicular (flat) or parallel (on-edge) to the print bed. In total, seven specimen types were produced, with three replicates of each type to assess experimental repeatability. Twenty-one test specimens were tested using a universal testing machine, SUNS UTM4503. The loading speed was set at 20 mm/min, and a standard extensometer was used to measure the deformation during the uniaxial tensile process. Fig. B2(a) shows the material testing experimental setup. Material testing followed ASTM D790 standards, the fabricated test specimens are shown in Fig. B2(b). Figures B2(c) and B2(d) show representative average stress–strain curves for different printing orientations, as well as the stress–strain responses of all specimens with corresponding mean values and error bands. The error bars represent the standard deviation (STD). For clarity, error bands are omitted in Fig. B2(c). Analysis of Fig.B2(d) indicates that the FDM process parameters employed in this study did not induce significant stiffness anisotropy in the elastic modulus; however, the specimens exhibited markedly different plastic behaviours depending on the printing orientation. As modal analyses are performed within the linear-elastic regime, a linear-elastic material model for 3D-printed test pieces is appropriate. One-direction tensile tests yielded a Young's modulus of 2.113 ± 0.105 GPa and a Poisson's ratio of 0.3.

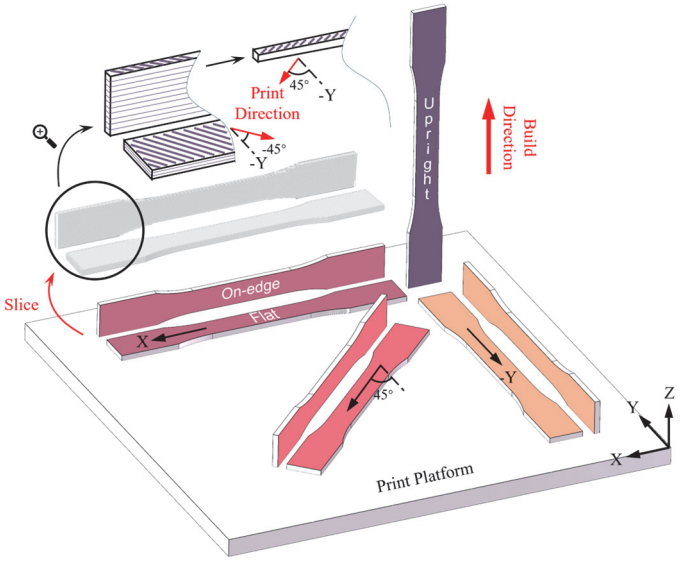

Figure B1. Process parameters and layer patterns for standardized test specimens

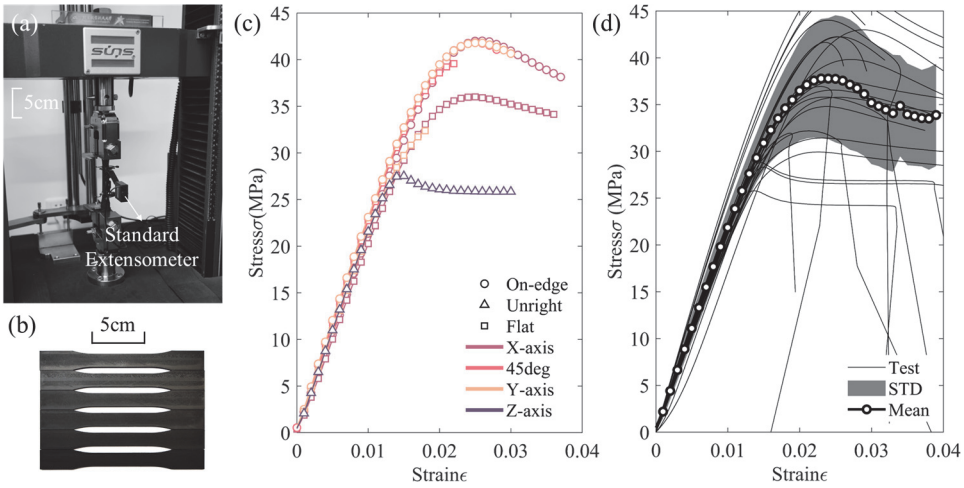

Figure B2. Mechanical properties testing: (a) Experimental setup. (b) Test specimens. (c) Representative stress–strain curves for different printing orientations. (d) Mean stress–strain curves of all specimens with error bands.

References

[1] S. Barbarino, O. Bilgen, R.M. Ajaj, M.I. Friswell, D.J. Inman, A Review of Morphing Aircraft, Journal of Intelligent Material Systems and Structures, 22 (2011) 823-877.

[2] D. Li, S. Zhao, A. Da Ronch, J. Xiang, J. Drofelnik, Y. Li, L. Zhang, Y. Wu, M. Kintscher, H.P. Monner, A. Rudenko, S. Guo, W. Yin, J. Kirn, S. Storm, R.D. Breuker, A review of modelling and analysis of morphing wings, Progress in Aerospace Sciences, 100 (2018) 46-62.

[3] R.M. Ajaj, E.I.S. Flores, M.I. Friswell, G. Allegri, B.K.S. Woods, A.T. Isikveren, W.G. Dettmer, The Zigzag wingbox for a span morphing wing, Aerospace Science and Technology, 28 (2013) 364-375.

[4] G. Wu, Y. Tong, J. Zhang, Z. Zhao, Design and dynamic analysis of a spanwise morphing wing for Mars exploration, Aerospace Science and Technology, 155 (2024) 109586.

[5] R.M. Ajaj, M.I. Friswell, M. Bourchak, W. Harasani, Span morphing using the GNATSpar wing, Aerospace Science and Technology, 53 (2016) 38-46.

[6] D.M. Boston, A.F. Arrieta, Multistable Honeycomb Architecture for Spanwise Wing Morphing, AIAA Scitech 2021 Forum, 2021.

[7] X. Guo, S. Wang, Y. Qu, D. Cao, Nonlinear dynamics of Z-shaped morphing wings in subsonic flow, Aerospace Science and Technology, 119 (2021) 107145.

[8] H. Gu, F. Healy, S. Jayatilake, D. Rezgui, M. Lowenberg, J. Cooper, T. Wilson, A. Castrichini, Flight dynamics of aircraft incorporating the semi-aeroelastic hinge, Aerospace Science and Technology, 147 (2024) 109026.

[9] X. Zhu, J. Zhang, W. Chen, H. Gu, Tension-twist coupling morphing wing using a novel mechanical metamaterial, Aerospace Science and Technology, 155 (2024) 109745.

[10] C. Wang, H.H. Khodaparast, M.I. Friswell, Conceptual study of a morphing winglet based on unsymmetrical stiffness, Aerospace Science and Technology, 58 (2016) 546-558.

[11] J.H.S. Fincham, M.I. Friswell, Aerodynamic optimisation of a camber morphing aerofoil, Aerospace Science and Technology, 43 (2015) 245-255.

[12] C. Wang, Y. Zhao, K. Huang, J. Zhang, A.D. Shaw, H. Gu, M. Amoozgar, M.I. Friswell, B.K.S. Woods, Integration of the passive energy balancing based actuation system into a camber morphing design, Aerospace Science and Technology, 155 (2024) 109641.

[13] Y. Wu, J. Li, Y. Dai, Y. Li, C. Yang, Active maneuver load alleviation for a pitching wing via spanwise-distributed camber morphing, Aerospace Science and Technology, 155 (2024) 109693.

[14] T. Mkhoyan, N.R. Thakrar, R. De Breuker, J. Sodja, Morphing wing design using integrated and distributed trailing edge morphing, Smart Materials and Structures, 31 (2022) 125025.

[15] A.C. Henry, G. Molinari, J.R. Rivas-Padilla, A.F. Arrieta, Smart Morphing Wing: Optimization of Distributed Piezoelectric Actuation, AIAA Journal, 57 (2019) 2384-2393.

[16] R.M. Ajaj, C.S. Beaverstock, M.I. Friswell, Morphing aircraft: The need for a new design philosophy, Aerospace Science and Technology, 49 (2016) 154-166.

[17] S. Vasista, L. Tong, K.C. Wong, Realization of Morphing Wings: A Multidisciplinary Challenge, Journal of Aircraft, 49 (2012) 11-28.

[18] A.E. Rivero, S. Fournier, M. Manolesos, J.E. Cooper, B.K.S. Woods, Experimental Aerodynamic Comparison of Active Camber Morphing and Trailing-Edge Flaps, AIAA Journal, 59 (2021) 2627-2640.

[19] D.A. Burdette, J.R.R.A. Martins, Design of a transonic wing with an adaptive morphing trailing edge via aerostructural optimization, Aerospace Science and Technology, 81 (2018) 192-203.

[20] Z. Lyu, J.R.R.A. Martins, Aerodynamic Shape Optimization of an Adaptive Morphing Trailing-Edge Wing, Journal of Aircraft, 52 (2015) 1951-1970.

[21] R. Pecora, Morphing wing flaps for large civil aircraft: Evolution of a smart technology across the Clean Sky program, Chinese Journal of Aeronautics, 34 (2021) 13-28.

[22] J. Xiang, Y. Yan, D. Li, Recent advance in nonlinear aeroelastic analysis and control of the aircraft, Chinese Journal of Aeronautics, 27 (2014) 12-22.

[23] R.K. Kapania, Y.H. Liu, Static and vibration analyses of general wing structures using equivalent-plate models, AIAA Journal, 38 (2000) 1269-1277.

[24] R. Vepa, Aeroelastic analysis of wing structures using equivalent plate models, AIAA Journal, 46 (2008) 1216-1225.

[25] F.H. Gern, D.J. Inman, R.K. Kapania, Structural and aeroelastic modeling of general planform wings with morphing airfoils, AIAA Journal, 40 (2002) 628-637.
[26] C. Spada, F. Afonso, F. Lau, A. Suleman, Nonlinear aeroelastic scaling of high aspect-ratio wings, Aerospace Science and Technology, 63 (2017) 363-371.
[27] H. Gu, F. Healy, D. Rezgui, J. Cooper, Sizing of High-Aspect-Ratio Wings with Folding Wingtips, Journal of Aircraft, 60 (2023) 461-475.
[28] D. Cao, C. Gao, X. Zhou, Y. Zhou, J. Wang, X. Guo, Flutter Analysis and Morphing Evaluation of Biomimetic Wing Structure, AIAA Journal, 63 (2024) 2463-2473.
[29] Q. Zou, R. Huang, X. Mu, Y. Li, H. Hu, H. Liu, Y. Zhao, Breaking Through Flutter Barrier of Rigid-Elastic Coupling Aircraft, Applied Mechanics Reviews, 78 (2025) 020801.
[30] X. Zhou, R. Huang, S. Yu, Z. Fan, H. Hu, Study on transient aeroelastic vibration and vehicle-mounted test for a morphing aircraft, Journal of Sound and Vibration, 623 (2026) 119505.
[31] W. Zhao, A. Gupta, C.D. Regan, J. Miglani, R.K. Kapania, P.J. Seiler, Component data assisted finite element model updating of composite flying-wing aircraft using multi-level optimization, Aerospace Science and Technology, 95 (2019) 105486.
[32] C.-g. Pak, S. Truong, Creating a Test-Validated Finite-Element Model of the X-56A Aircraft Structure, Journal of Aircraft, 52 (2015) 1644-1667.
[33] O. Avin, D.E. Raveh, A. Drachinsky, Y. Ben-Shmuel, M. Tur, Experimental Aeroelastic Benchmark of a Very Flexible Wing, AIAA Journal, 60 (2022) 1745-1768.
[34] C. Riso, C.E.S. Cesnik, Impact of Low-Order Modeling on Aeroelastic Predictions for Very Flexible Wings, Journal of Aircraft, 60 (2023) 662-687.
[35] J.R. Wright, J.E. Cooper, Introduction to aircraft aeroelasticity and loads, John Wiley & Sons2008.
[36] R. Pecora, M. Magnifico, F. Amoroso, E. Monaco, Multi-parametric flutter analysis of a morphing wing trailing edge, The Aeronautical Journal, 118 (2016) 1063-1078.
[37] Q. Zou, R. Huang, X. Mu, H. Hu, Z. Fan, H. Liu, Body-freedom flutter analysis and flight test for a flying-wing aircraft testbed, Mechanical Systems and Signal Processing, 221 (2024) 111717.
[38] E. Jonsson, C. Riso, C.A. Lupp, C.E.S. Cesnik, J.R.R.A. Martins, B.I. Epureanu, Flutter and post-flutter constraints in aircraft design optimization, Progress in Aerospace Sciences, 109 (2019) 100537.
[39] Q. Zou, R. Huang, H. Hu, H. Liu, Studying body-freedom flutter mechanism via a rigid-elastic aeroelastic model of reduced-order, Aerospace Science and Technology, 161 (2025) 110155.
[40] R.L. Bisplinghoff, H. Ashley, R.L. Halfman, Aeroelasticity, Courier Corporation2013.
[41] A. Hossein Modaress-Aval, F. Bakhtiari-Nejad, E.H. Dowell, H. Shahverdi, D. Peters, Comparative Study of Beam and Plate Theories for Moderate Aspect Ratio Wings, AIAA Journal, 61 (2023) 859-874.
[42] A.H. Modaress-Aval, F. Bakhtiari-Nejad, E.H. Dowell, D.A. Peters, H. Shahverdi, A comparative study of nonlinear aeroelastic models for high aspect ratio wings, Journal of Fluids and Structures, 85 (2019) 249-274.
[43] T. Theodorsen, General Theory of Aerodynamic Instability and the Mechanism of Flutter, NACA, 1934.
[44] T. Theodorsen, I. Garrick, Mechanism of flutter: a theoretical and experimental investigation of the flutter problem, NACA Langley Field, VA, USA1940.
[45] W.P. Walker, M.J. Patil, Unsteady Aerodynamics of Deformable Thin Airfoils, Journal of Aircraft, 51 (2014) 1673-1680.
[46] M. Mesarič, F. Kosel, Unsteady airload of an airfoil with variable camber, Aerospace Science and Technology, 8 (2004) 167-174.
[47] C.Y. Herrera, N.D. Spivey, S.-f. Lung, Aeroelastic Response of the Adaptive Compliant Trailing Edge Transtition Section, 2016.
[48] K. Soneda, T. Yokozeki, T. Imamura, N. Tsushima, Multifidelity Aeroelastic Model for Corrugated Morphing Structures, Journal of Aircraft, 60 (2023) 120-129.
[49] R. De Breuker, M.M. Abdalla, Z. Gurdal, Flutter of Partially Rigid Cantilevered Two-Dimensional Plates in Axial Flow, AIAA Journal, 46 (2008) 936-946.
[50] R. Drazumeric, B. Gjerek, F. Kosel, P. Marzocca, On bimodal flutter behavior of a flexible airfoil, Journal of Fluids and Structures, 45 (2014) 164-179.

[51] J. Zhang, A.D. Shaw, C. Wang, H. Gu, M. Amoozgar, M.I. Friswell, B.K.S. Woods, Aeroelastic model and analysis of an active camber morphing wing, Aerospace Science and Technology, 111 (2021) 106534.
[52] D.M. Tang, H. Yamamoto, E.H. Dowell, Flutter and limit cycle oscillations of two-dimensional panels in three-dimensional axial flow, Journal of Fluids and Structures, 17 (2003) 225-242.
[53] Z.Y. Hu, L. Liang, Y.Q. Shi, R. Li, A new analytical framework for free vibration solutions of rectangular plates with internal discontinuities, Aerospace Science and Technology, 153 (2024) 109453.
[54] J. Katz, Low-speed aerodynamics, Cambridge University Press2001.
[55] A. Concilio, I. Dimino, R. Pecora, SARISTU: adaptive trailing edge device (ATED) design process review, Chinese journal of aeronautics, 34 (2021) 187-210.
[56] J.J. Joo, C.R. Marks, L. Zientarski, Active wing shape reconfiguration using a variable camber compliant wing system, 20th International Conference on Composite Materials, Copenhagen, Denmark, 2015, pp. 19-24.
[57] S.B. Cumming, M.S. Smith, A. Ali, T.T. Bui, J. Ellsworth, C.A. Garcia, Aerodynamic Flight Test Results for the Adaptive Compliant Trailing Edge, AIAA Atmospheric Flight Mechanics Conference, 2016.
[58] A.E. Rivero, P.M. Weaver, J.E. Cooper, B.K.S. Woods, Structural Modeling of Compliance-Based Camber Morphing Structures Under Transverse Shear Loading, AIAA Journal, 58 (2020) 4941-4951.
[59] S. Yu, X. Zhou, R. Huang, Time-Varying Aeroelastic Modeling and Analysis for a Morphing Wing, AIAA Journal, 62 (2024) 3825-3840.
[60] J.M. Chacón, M.A. Caminero, E. García-Plaza, P.J. Núñez, Additive manufacturing of PLA structures using fused deposition modelling: Effect of process parameters on mechanical properties and their optimal selection, Materials & Design, 124 (2017) 143-157.
[61] M. Somireddy, A. Czekanski, Anisotropic material behavior of 3D printed composite structures – Material extrusion additive manufacturing, Materials & Design, 195 (2020) 108953.
[62] N. Khan, A. Riccio, A systematic review of design for additive manufacturing of aerospace lattice structures: Current trends and future directions, Progress in Aerospace Sciences, 149 (2024) 101021.
[63] U. Fasel, D. Keidel, L. Baumann, G. Cavolina, M. Eichenhofer, P. Ermanni, Composite additive manufacturing of morphing aerospace structures, Manufacturing Letters, 23 (2020) 85-88.
[64] S.J. Rothberg, M.S. Allen, P. Castellini, D. Di Maio, J.J.J. Dirckx, D.J. Ewins, B.J. Halkon, P. Muyshondt, N. Paone, T. Ryan, H. Steger, E.P. Tomasini, S. Vanlanduit, J.F. Vignola, An international review of laser Doppler vibrometry: Making light work of vibration measurement, Optics and Lasers in Engineering, 99 (2017) 11-22.
[65] A.H. Nayfeh, Linear and nonlinear structural mechanics, John Wiley & Sons2024.
[66] A.W. Leissa, The free vibration of rectangular plates, Journal of Sound and Vibration, 31 (1973) 257-293.
[67] K.M. Liew, K.Y. Lam, S.T. Chow, Free vibration analysis of rectangular plates using orthogonal plate function, Computers & Structures, 34 (1990) 79-85.
[68] Y.J. Liu, G.R. Buchanan, Free vibration of stepped cantilever Mindlin plates, Journal of Sound and Vibration, 271 (2004) 1083-1092.
[69] R. Plunkett, Natural frequencies of uniform and non-uniform rectangular cantilever plates, Journal of Mechanical Engineering Science, 5 (1963) 146-156.
[70] J.W. Dalley, E.A. Ripperger, Experimental values of natural frequencies for skew and rectangular cantilever plates, Proceedings of the Society of Experimental Stress Analysis, 9 (1952) 51-66.
[71] D. Systèmes, SIMULIA User Assistance 2024, Dassault Systèmes Simulia Corp., Johnston, RI, 2024.
[72] G. Martin, E. Balmes, T. Chancelier, Characterization of identification errors and uses in localization of poor modal correlation, Mechanical Systems and Signal Processing, 88 (2017) 62-80.
[73] D. Ahmad, M.S. Parancheerivilakkathil, A. Kumar, M. Goswami, R.M. Ajaj, K. Patra, M. Jawaid, K. Volokh, Y. Zweiri, Recent developments of polymer-based skins for morphing wing applications, Polymer Testing, 135 (2024) 108463.
[74] C.J. Hunt, F. Morabito, C. Grace, Y. Zhao, B.K.S. Woods, A review of composite lattice structures, Composite Structures, 284 (2022) 115120.